



Vanadium tuning amorphous iron phosphate encapsulated iron phosphide on phosphorous-doped graphene promoted oxygen reactions for flexible zinc air batteries

Quynh Phuong Ngo^a, Thanh Tuan Nguyen^a, Manjinder Singh^a, Ravichandran Balaji^a,
Nam Hoon Kim^{a,*}, Joong Hee Lee^{a,b,**}

^a Department of Nano Convergence Engineering (BK21 FOUR), Jeonbuk National University, Jeonju, Jeonbuk 54896, Republic of Korea

^b Carbon Composite Research Center, Department of Polymer-Nanoscience and Technology, Jeonbuk National University, Jeonju, Jeonbuk 54896, Republic of Korea

ARTICLE INFO

Keywords:

Heterostructure
Vanadium iron
Phosphide
Catalyst
Zinc air battery

ABSTRACT

The zinc air batteries (ZABs) are emerging as potential energy storage devices, because of its low-cost, safety, and high energy density. The oxygen evolution reaction (OER) and oxygen reduction reaction (ORR) mainly occur at the air-cathode, which play the key role in the ZAB's performance. However, the sluggish oxygen reactions require an overpotential and multiple electron transfer steps. Herein, the unique crystalline/amorphous nano-structure of V-doped Fe₂P/FePO_x@PG hybrid has been prepared, which showed the electronic structure tuning and synergistic effect. The catalyst exhibited a small overpotential of 270 mV at 10 mA cm⁻² for OER, and a high half-wave potential of 0.84 V for ORR. When serving as air-cathode for ZABs, it showed ultralong durability of 600 h with high peak power density of 137 mW cm⁻². The solid-state ZABs demonstrated superior performance with different testing conditions, offering high potential to apply to the next generation flexible energy storage devices.

1. Introduction

The next generation energy storage systems are the most important components for electronic devices in modern life and human society [1, 2]. The Zinc-air battery (ZAB) is well-known as an economical energy storage device, owing to its cost-effectiveness, high energy density, and safety [3–6]. Nevertheless, the performance of the ZAB is regulated by two critical oxygen reactions, i.e., the oxygen reduction reaction (ORR) during discharge, and the oxygen evolution reaction (OER) during charge processes. However, the ORR and OER require multiple electron transfer steps that exhibit slow kinetics, which lead to the low-rate performance for ZABs and large polarization. The rational design of efficient catalysts, which could provide more active sites, activate the oxygen molecules, and improve the kinetics at the electrolyte boundary, is essential [7–9]. Platinum group metals (PGMs) are the state-of-the-art electrocatalysts for ORR and OER; however, the irreversibility, scarcity, and expense of PGMs has hindered them from wide use in industrial applications [10–13]. In addition, the complexity for fabrication of two

different catalysts (OER and ORR) in an air cathode is another challenge that could increase the installation and operation cost [14,15]. Therefore, a suitable strategy to develop efficient and low-cost electrocatalyst for the air cathode is needed, which may boost the ORR and OER activities, and enhance the performance of ZABs.

Transition metal-based materials, such as sulfide, phosphide, nitride, and selenide, have attracted attention due to their high catalytic activities, low-cost, abundance in nature, and tunable nanostructures [16–19]. However, these oxygen reaction catalysts suffer from oxidation, stripping/deposition, or rearrangement of their nanostructure during the working process, which could reduce their catalytic activities and long-term stability. Carbon-based material is an encouraging candidate to prevent the degradation of electrocatalyst activity due to its exceptional electronic conductivity and long-term stability [20–23]. The encapsulation of carbon-based materials with metal active sites could generate an outstanding electron transport channel, promote the synergistic effect between core active sites and stable carbon shell, and therefore could enhance the oxygen reaction kinetics [24,25]. For

* Corresponding author.

** Corresponding author at: Department of Nano Convergence Engineering (BK21 FOUR), Jeonbuk National University, Jeonju, Jeonbuk 54896, Republic of Korea.
E-mail addresses: nhk@jbnu.ac.kr (N.H. Kim), jhl@jbnu.ac.kr (J.H. Lee).

<https://doi.org/10.1016/j.apcatb.2023.122674>

Received 15 November 2022; Received in revised form 2 March 2023; Accepted 21 March 2023

Available online 22 March 2023

0926-3373/© 2023 Elsevier B.V. All rights reserved.

example, Zhang et al. prepared WN–Ni Mott–Schottky heterogenous catalysts encapsulated into N, P doped CNT, which served as an outstanding air cathode for ZABs [26]. Shi and co-workers constructed bifunctional $\text{Co}_x\text{P} @ \text{N,P-doped carbon}$ to boost ORR/OER catalytic activities, which outperformed the benchmark $\text{Pt/C}–\text{RuO}_2$ catalyst. The $\text{Co}_x\text{P} @ \text{N,P-doped carbon}$ air cathode-based ZABs showed high peak power density and long-term cycle life [27]. However, the catalytic activities degrade due to oxidation, which might reduce the long-term use of catalyst, and hinder their practical application. The appropriate design nanostructures with oxygen atom electronic coupling at interfaces could enhance the active sites (the components react with $^*\text{OH}$, $^*\text{O}$, $^*\text{OO}$, and $^*\text{OOH}$), and improve the lifetime of catalysts. In this case, adjustment of O–O bonding is one of the most efficient ways to monitor the adsorption energy and further accelerate the oxygen reactions [28–30].

Herein, we anticipated a novel strategy to formulate a series of metal phosphide/phosphates, protected by phosphorous-doped graphene nanosheet. The combination of metal phosphide and phosphate demonstrated superior catalysis performance, compared to its counterparts. The appearance of phosphate amorphous phase as a miniature cluster could increase the catalytical active sites, in comparison to the high crystallinity of phosphide materials [31]. The numerous active sites could boost the intermediates absorbance species for OER, and therefore accelerate the oxygen reactions. In addition, during the electrochemical performance, the unavoidable oxidation on the catalyst surface could convert phosphide into the corresponding phosphate. This process could form the linker coordinator and chelation effect of active nucleation core, therefore enhancing the activity of catalysts.

The optimize V–doped $\text{Fe}_2\text{P}/\text{FePO}_x$ heterostructures encapsulated in phosphorous graphene (V– $\text{Fe}_2\text{P}/\text{FePO}_x @ \text{PG}$) was demonstrated as a highly effective catalyst for ORR and OER. As an outstanding catalyst for ORR, a high onset potential was obtained of 0.94 V, and remarkable half-wave potential ($E_{1/2}$) of 0.84 V. Moreover, a low overpotential of 270 mV is required when V– $\text{Fe}_2\text{P}/\text{FePO}_x @ \text{PG}$ is used as OER catalyst, which is superior to its counterparts and current reports in the literature [32]. When applied as cathode for zinc air batteries, the as-obtained devices present a notable cell voltage of 1.424 V with long-term durability of 600 h and high-power density of 137 mW cm^{-2} . In addition, the flexible ZABs demonstrated excellent physical properties and exceptional durability in various testing conditions, confirming that the new strategy could provide a potential way to apply the ZAB in wearable and flexible electronics.

2. Experimental section

2.1. Chemicals

All chemicals were purchased from Sigma–Aldrich and were used directly without further purification.

2.2. Synthesis of V– $\text{Fe}_2\text{P}/\text{FePO}_x @ \text{PG}$

Graphene oxide was first prepared by a modified Hummer method, as per our previous report [33]. Next, 50 mg of GO was redispersed in 50 mL of deionized water using ultrasonication for 60 min. The 0.5 mmol of $\text{Fe}(\text{NO}_3)_3 \cdot 6\text{H}_2\text{O}$ and 0.05 mmol of VOSO_4 were dissolved in 2 mL DI water, followed by dropwise addition into the above GO solution, and stirring for 20 min. Afterward, 2.0 mL of phytic acid (PA) was slowly dropped into the solution under vigorous stirring. The reaction was continuously carried out at 90°C for 12 h, and the mixture was freeze-dried at -80°C for 2 days. The powder was then pyrolyzed at 900°C under Ar/H_2 atmosphere (ratio 9:1) for 2 h, to obtain the V– $\text{Fe}_2\text{P}/\text{FePO}_x @ \text{PG}$. For comparison, the $\text{Fe}_2\text{P}/\text{FePO}_x @ \text{PG}$, V– $\text{Fe}_2\text{P}/\text{FePO}_x$, and PG were prepared using a similar procedure without corresponding material sources.

2.3. Material characterization

The morphology of materials was inspected using field emission scanning electron microscopes (FE-SEM) (JEOL JSM-6701 F, Japan) and transmission electron microscopy (TEM) (JEM-ARM200F (JEOL, Japan)) at the Center for University-Wide Research Facilities (CURF), Jeonbuk National University (JBNU). The X-ray diffraction (XRD) patterns were collected using a Rigaku Ultima IV (Japan) with $\text{Cu-K}\alpha$ radiation ($\lambda = 0.154 \text{ nm}$) at a scanning rate of 2°C . The elemental composition was collected with an EDAX (SUPRA 40 VP; Carl Zeiss, Germany). The specific surface area and pore size distribution were obtained from the Brunauer–Emmett–Teller (BET) theory and Barrett–Joyner–Halenda (BJH) method using a Micromeritics ASAP 2020 at $\sim 77 \text{ K}$. The binding energy was analyzed using an X-ray photoelectron spectroscopy (XPS) (Thermo Fisher Scientific, UK) at KBSI, Jeonju. Raman spectroscopy was examined using a Nanofinder–30 instrument (Tokyo Instruments Co., Japan) with 532 nm laser. The electrical conductivity was measured using the four-point probe technique (MS Tech four-probe station; Keithly 2182 A).

2.4. Electrochemical measurements

The electrochemical performance of catalysts was examined using a CHI760E workstation (CH Instruments Inc., USA). A carbon rod was used as the counter electrode, and Hg/HgO electrode as a reference electrode. A nickel foam (NF) piece of $1 \text{ cm} \times 1 \text{ cm}$ size was pretreated with HCl 1 M and washed out with water and ethanol to remove the oxide layer and further used as a current collector to analyze the OER performance. In detail, 8 mg of as-prepared catalyst, 1 mg of carbon black, and 1 mg of PVDF binder were dispersed into 1 mL of NMP. The solution was further sonicated for 30 min, coated onto the NF, then dried at 60°C for 6 h in vacuum oven. Moreover, we coated the as-prepared catalysts on the carbon cloth substrate with similar procedure and carried out the OER performance for comparison. For ORR performance, the working electrode was prepared by drop-casting $7 \mu\text{L}$ of catalysts ink including 3 mg of materials and $5 \mu\text{L}$ in $250 \mu\text{L}$ ethanol and water (v/v 1:1) onto a glassy carbon rotating disk electrode (RDE).

All potential was converted to the RHE using the Nernst equation, as follows:

$$E_{\text{RHE}} = E_{\text{measure}} + E_{\text{Hg}/\text{HgO}}^\circ + 0.059 \times \text{pH} \quad (1)$$

The hydrogen peroxide yields and the electron transfer number (n) were estimated using the rotating ring disk electrode (RRDE) method, and calculated as the following equation:

$$\text{H}_2\text{O}_2(\%) = 200 \times \frac{I_{\text{R}}/N}{I_{\text{R}}/N + I_{\text{D}}} \quad (2)$$

$$n = 4 \times \frac{I_{\text{D}}}{I_{\text{D}} + I_{\text{R}}/N} \quad (3)$$

where, I_{R} and I_{D} are the ring and disk currents, respectively, and N is the collection coefficient.

2.5. Zinc–air battery measurements

The zinc–air battery performance was investigated with a homemade cell. The air electrode was prepared by uniformly coating the as-prepared catalyst ink onto a carbon cloth with a gas diffusion layer and dried at 60°C overnight. The mass loading was fixed at 0.5 mg cm^{-2} . A polished Zn plate with a thickness of 0.25 mm was used as the anode. An aqueous solution consisting of 0.2 M Zn (CH_3CO_2) $_2 \cdot 2\text{H}_2\text{O}$ and 6 M KOH was used as the electrolyte. For solid-state zinc-air battery, the polyvinyl alcohol (PVA)/KOH gel was prepared as described in our previous report [34]. In detail, 5 g PVA was dissolved in 50 mL of 6 M KOH contained 0.2 M Zn(CH_3CO_2) $_2 \cdot 2\text{H}_2\text{O}$ and

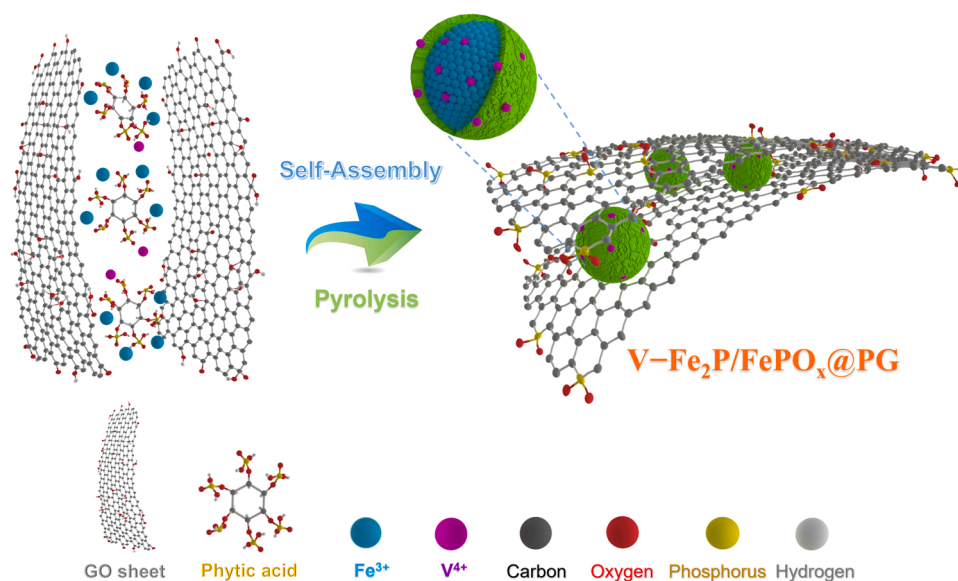


Fig. 1. Schematic for the fabrication of $\text{V-Fe}_2\text{P/FePO}_x\text{@PG}$.

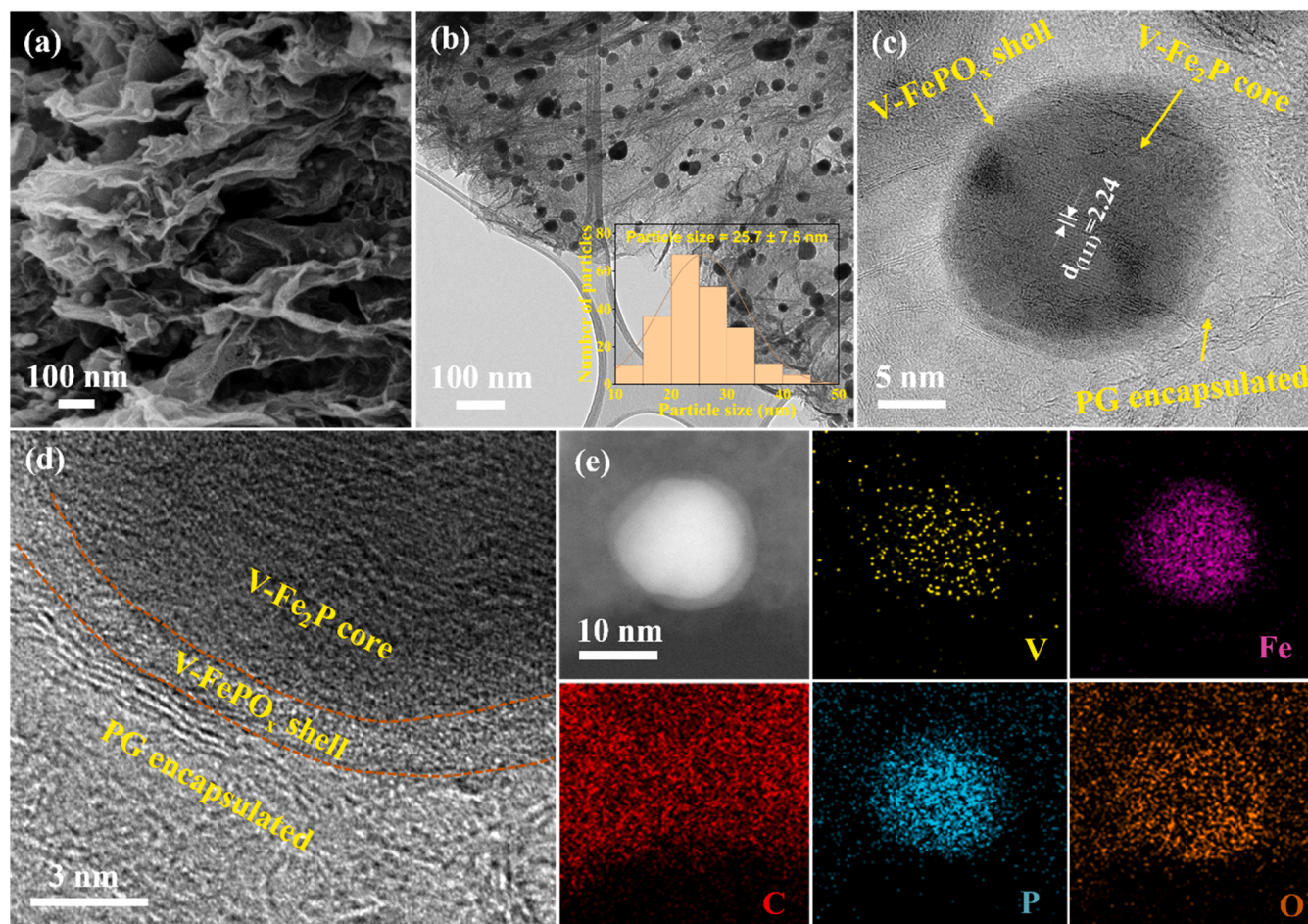


Fig. 2. Morphological characterization: (a) FE-SEM image; (b-d) Low and high-magnification TEM images, and (e) STEM-EDS color mapping of the $\text{V-Fe}_2\text{P/FePO}_x\text{@PG}$ with the V, Fe, C, P, and O elements distribution.

keep stirring for 12 h at 85 °C. After that, the mixture was poured on a petri-disc and stored in the freezer to obtain the PVA/KOH gel electrolyte.

2.6. Theoretical calculations

The CASTEP code was employed to carry out DFT calculation [35–37]. The generalized gradient approximation (GGA) and

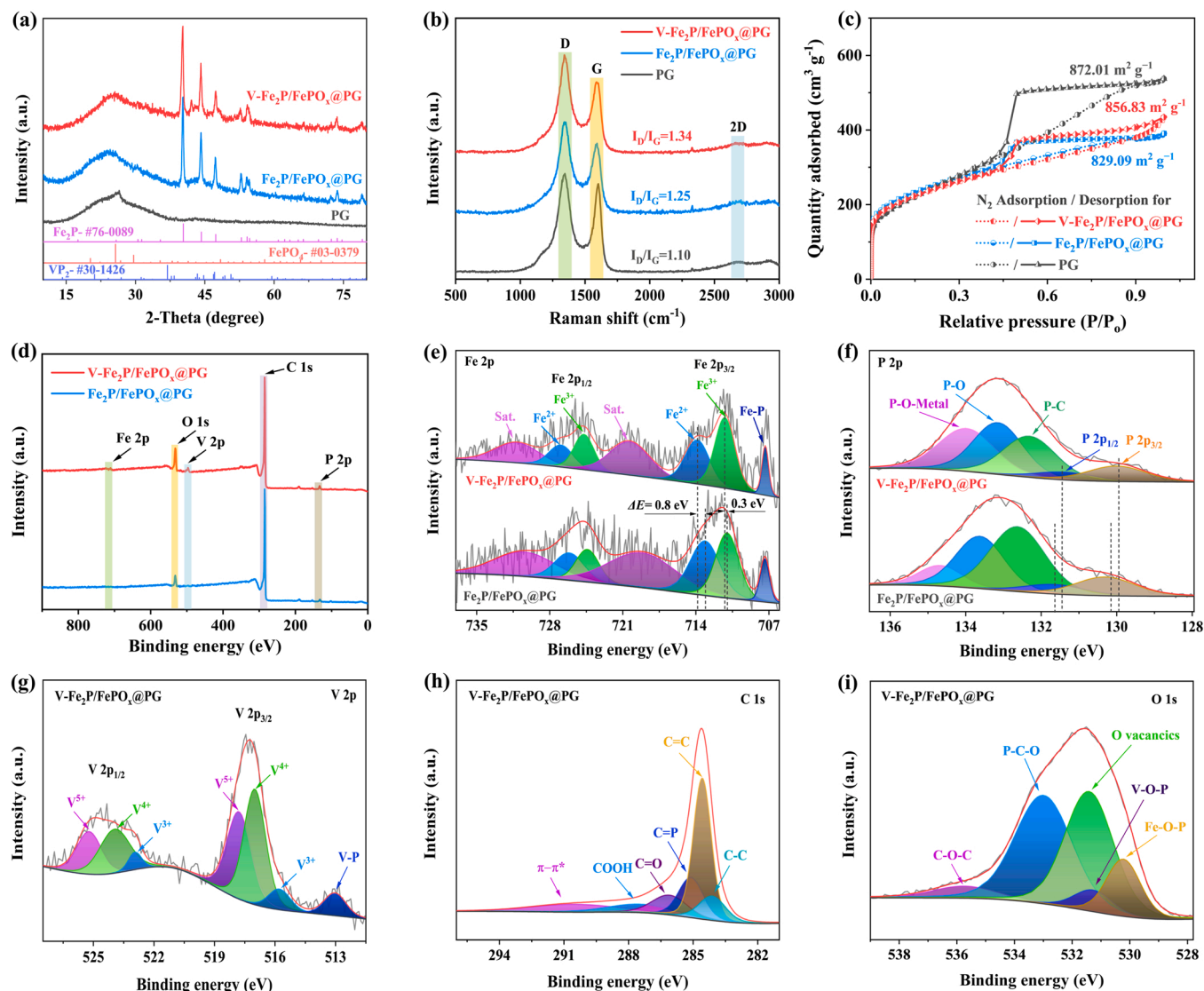


Fig. 3. Material characterization: (a) The XRD patterns, (b) Raman spectra, and (c) N₂ adsorption–desorption isotherms of the V–Fe₂P/FePO_x@PG, Fe₂P/FePO_x@PG, and PG catalysts; (d) XPS survey spectra, (e–f) high-resolution XPS spectra of Fe 2p and P 2p for V–Fe₂P/FePO_x@PG and Fe₂P/FePO_x@PG; and (g–i) The high-resolution XPS spectra of V 2p, C 1s, and O 1s for V–Fe₂P/FePO_x@PG.

Perdew–Burke–Ernzerhof (PBE) were used for exchange and correlation energy of electron. The plane-wave cutoff energy for all models was set at 300 eV [38–40].

The Gibb free energy was estimated by the calculation formular:

$$\Delta G = \Delta E + \Delta E_{\text{ZPE}} - T\Delta S \quad (4)$$

where ΔE is the optimizing energy difference of system, ΔE_{ZPE} and ΔS could be acquired by using the vibrational frequency calculation.

3. Results and discussions

3.1. Material characterization

Fig. 1 shows the facile self-assembly synthesis procedure of the V-doped Fe₂P/FePO_x@PG. The presence of phytic acid in the initial solution plays an important role in providing the phosphorous source for metal phosphide formation and doping to graphene oxide. The six phosphorous acid “arms” of the snowflake-like molecular structure of phytic acid will be transferred into organophosphates under the carbonization process, and generate the phosphate linkages [41]. Moreover, the doping of P atoms into graphene framework could

enhance the active sites and increase the electrochemical performance [42].

The physical characteristics of materials were analyzed using FE-SEM and TEM. Fig. 2a shows the very thin sheet of graphene with clear wrinkles, which could enhance the specific surface area and electrochemical performance of the catalysts [43]. The low-magnification TEM images in Fig. 2b shows the high uniformity of nanoparticles that are distributed around the graphene sheets. The average particle size was calculated as around 18–32 nm. The high-resolution TEM (HR-TEM) image of V–Fe₂P/FePO_x@PG nanostructures clearly shows the highly crystalline V–Fe₂P and amorphous V–FePO_x shell (Fig. 2c). The V–Fe₂P exhibited the lattice spacing of 2.24 Å related to the (111) plane of V–Fe₂P (ICDD#01–076–0089), which is consistent with the XRD results. Moreover, the several layers of PG shown in Fig. 2d further confirm the successful coating of PG on V–Fe₂P/FePO_x nanoparticles. The d-spacing of graphene layer was calculated as 3.5 Å, which is higher than the typical graphitic carbon (3.4 Å), due to the doping of the higher ionic radii of P into the graphene framework. The coating layer could inhibit the degradation of metal catalysts during OER/ORR performance. The scanning TEM (STEM) and corresponding EDS color mapping show the distribution of each element in the V–Fe₂P/FePO_x@PG

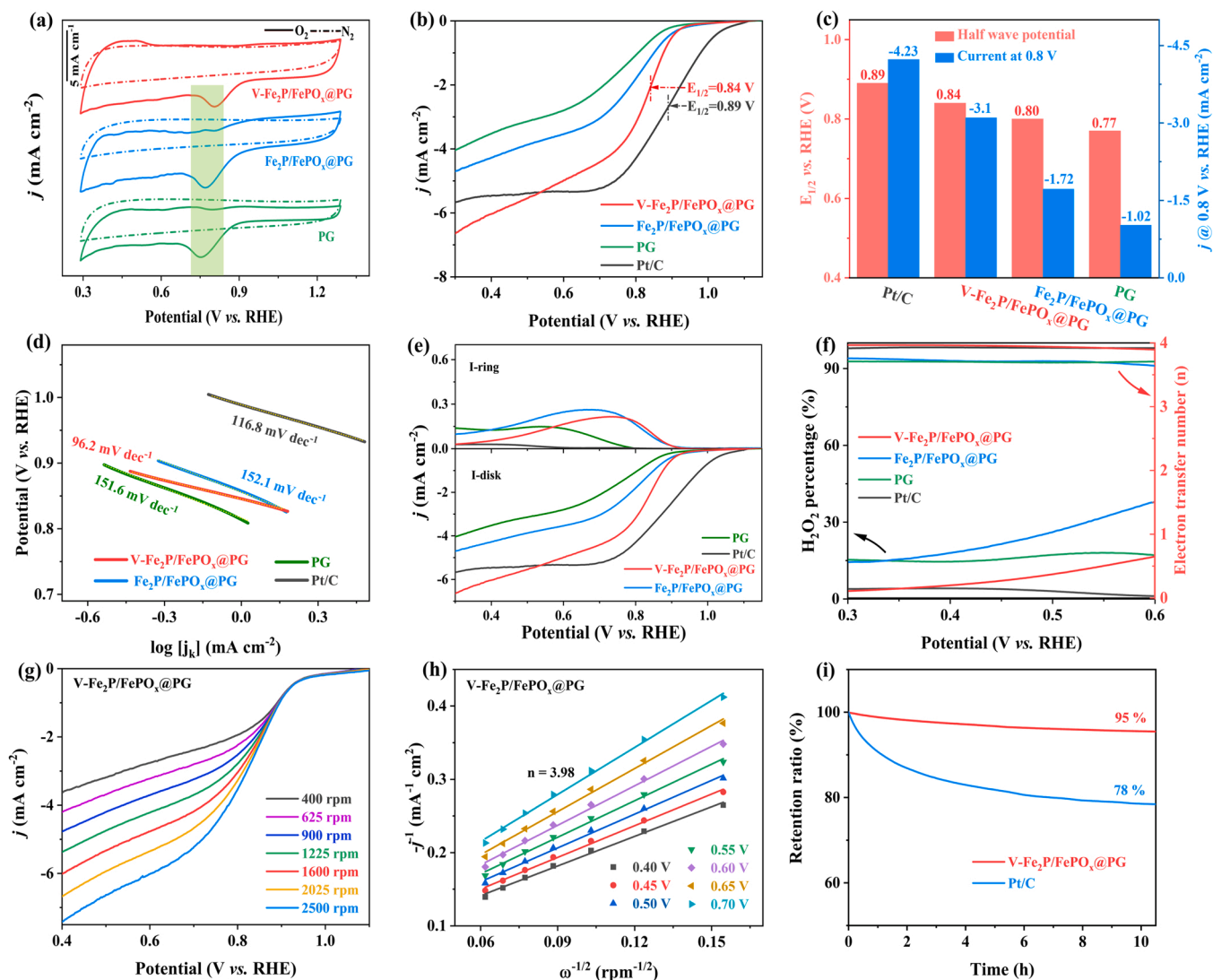


Fig. 4. (a) The CV curves of the V-Fe₂P/FePO_x@PG, Fe₂P/FePO_x@PG, and PG at a fixed scan rate of 50 mV s⁻¹ in N₂- and O₂-saturated 0.1 M KOH electrolyte; (b) LSV polarization curves with RDE; (c) The comparison of E_{1/2} and current density at 0.8 V; (d) Tafel plots derived from the LSV; (e) LSV curves with RRDE which display j_{disk} and j_{ring}; (f) H₂O₂ yield and the electron transfer number of the V-Fe₂P/FePO_x@PG, Fe₂P/FePO_x@PG, PG, and Pt/C catalysts in O₂-saturated 0.1 M KOH electrolyte; (g) LSV curves at various electrode rotation speeds; and (h) K-L plots of V-Fe₂P/FePO_x@PG; (i) The chronoamperometric stability of V-Fe₂P/FePO_x@PG and Pt/C catalysts.

core-shell nanostructures (Fig. 2e and S1). In addition, the SEM images of the other counterparts such as V-Fe₂P/FePO_x, Fe₂P/FePO_x@PG, and PG were accumulated for comparison (Fig. S2). The nanoparticles of V-Fe₂P/FePO_x was aggregated without the support of PG that confirmed the benefit of graphene nanosheets, it could uniform cover and protect the metal active nanoparticles. Although, the PG showed the uniformly crumpled nanosheets, which offered a high surface area and could be an effective substrate for electron transport and enhance electrochemical performance.

The XRD patterns were measured to analyze the crystallinity and nanostructure of the V-Fe₂P/FePO_x@PG. Fig. 3a shows the broad peak at 2θ ~25°, which could be attributed to the PG framework. The high-intensity peaks at 2θ ~40.1, 44.09, and 47.31° with a slight shift to the lower 2θ angle could be assigned to the (111), (201), and (210) facet planes of Fe₂P (ICDD#01-076-0089), respectively [44]. The shifting of peaks due to the cation exchange of a greater radius atom of V (0.64 Å) with a smaller atom Fe (0.58 Å) in V-Fe₂P crystal leads to a larger lattice distance in the V-Fe₂P/FePO_x@PG nanostructure. In addition, no extra diffraction peaks are observed, illustrating the high purity of V-Fe₂P/FePO_x@PG without the separating crystalline phases.

Raman spectra were employed to further analyze the crystal quality and defect information of the carbon-based materials. The Raman spectrum of GO showed two main typical peaks at 1356 and 1585 cm⁻¹, revealing the D and G band, respectively (Fig. S3) [45]. When the phosphorous atoms were doped into graphene sheet to form PG and V-Fe₂P/FePO_x@PG, the D band was shifted to lower value of 1342 and 1339 cm⁻¹, owing to the distortion of structure and defect sites generations in the carbon framework (Fig. 3b) [46]. Similarly, the G band of PG and V-Fe₂P/FePO_x@PG were shifted to 1602 and 1597 cm⁻¹, compared to GO (1585 cm⁻¹). The I_D/I_G ratio is a critical parameter to identify the crystal quality of carbon-based materials [47]. As shown in Fig. 3b and S3, the I_D/I_G increased from 0.92 to 1.10, 1.25, and 1.34 for GO, PG, Fe₂P/FePO_x@PG, and V-Fe₂P/FePO_x@PG, demonstrating the successful doping of P atoms into graphene network, which could enhance the defects in the framework. The doping of P into graphene network could enhance the active sites and increase the catalytic activities of the electrocatalysts.

To further investigate the specific surface area and porous nanostructure, we analyzed the BET N₂ adsorption/desorption isotherm of the as-prepared nanostructure (Fig. 3c) [48]. The typical type IV

sorption isotherm was obtained with the mesoporous nanostructure properties [49]. The estimated total BET specific surface area for the PG is high at $872.01 \text{ m}^2 \text{ g}^{-1}$, and is slightly reduced by the encapsulation of $\text{V-Fe}_2\text{P/FePO}_x \text{ @PG}$ ($856.83 \text{ m}^2 \text{ g}^{-1}$) and $\text{Fe}_2\text{P/FePO}_x \text{ @PG}$ ($829.09 \text{ m}^2 \text{ g}^{-1}$). This result is due to some inevitable agglomeration of metal phosphide when it was formed and distributed in the graphene network [50]. Fig. S4 shows the pore distribution with the diameter of around 4 nm for the as-prepared nanostructures, which could enhance the catalytic active sites, and improve the mass transfer for oxygen reactions.

To examine the binding composition and elemental valence state of nanostructure, we investigated the XPS. Fig. 3d shows the survey spectrum of $\text{V-Fe}_2\text{P/FePO}_x \text{ @PG}$, which clearly demonstrates the appearance of V, Fe, P, C, and O elements. The XPS of Fe 2p could be deconvoluted into three coupled peaks of Fe $2p_{3/2}$ of 711.2 and 713.8 eV and Fe $2p_{1/2}$ of 724.7 and 726.9 eV, with the corresponding satellite peaks positioned at binding energy of 720.4 and 731.2 eV, respectively (Fig. 3e) [51]. When the V atom was doped, the Fe $2p_{3/2}$ peak of $\text{V-Fe}_2\text{P/FePO}_x \text{ @PG}$ was slightly shifted to the positive side, compared to the $\text{Fe}_2\text{P/FePO}_x \text{ @PG}$ (Fig. 3e). The shifting phenomenon due to the vanadium doping could provide the higher valence state of iron ion. The XPS spectra of P 2p exhibited the M–P and M– PO_x bond at the binding energy of 129.6 and 130.6 eV, respectively, demonstrating the formation of phosphide and phosphate compounds (Fig. 3f) [52]. In addition, the peaks at binding energy of 132.3 eV associated with the P–C binding further demonstrated the doping of P atoms into carbon network [53]. The high-resolution XPS spectra of V 2p shows three main peaks located at binding energy of 515.7, 516.9, and 517.7 eV, which are assigned to V^{3+} , V^{4+} , and V^{5+} , respectively (Fig. 3g). The peak located at binding energy of 512.9 eV validated the existence of V–P bonding in the $\text{V-Fe}_2\text{P/FePO}_x \text{ @PG}$ nanostructures [54]. On the other hand, the deconvolution spectrum of C 1s showed the peaks at ~ 284.2 , 284.6, 285.2, 285.8, 288.3, and 291.4 eV, related to the C–C, C=C, C=P, C=O, COOH, and π - π * bonds, respectively (Fig. 3h). This result illustrates the successful doping of P into PG framework [55]. The O 1s could be deconvoluted into the different peaks at ~ 530.3 , 531.1, 531.3, 532.8, and 536.0 eV, corresponding to Fe–O–P, V–O–P, O vacancies, P–C–O, and C–O–C, respectively. The broad peak at 536.0 eV is due to unavoidable moisture adsorption on the surface of hybrid material, suggesting the strong hydrophilic nature of the as-prepared catalysts (Fig. 3i) [56].

3.2. Electrochemical measurement

The ZAB performance is mainly affected by two opposite oxygen reactions (i.e., the oxygen evolution reaction and the oxygen reduction reaction). To employ the material as efficient air cathode for zinc air battery, we first investigated the ORR and OER performance.

3.2.1. ORR performance

To examine the electrochemical performance of the catalyst for ORR, we performed cyclic voltammetry (CV) measurement in both saturated N_2 and O_2 atmosphere with three-electrode configuration. The $\text{V-Fe}_2\text{P/FePO}_x \text{ @PG}$ catalyst ink was cast on a rotation disk electrode as working electrode, Hg/HgO and graphite rod were used as reference electrode and counter electrode, respectively [57]. Fig. 4a shows the CV curve with N_2 -saturated solution, which reveals no redox peak, while that with the O_2 -saturated solution exhibited a well-defined peak at potential of 0.81 V, demonstrating the high catalytic activities of the $\text{V-Fe}_2\text{P/FePO}_x \text{ @PG}$ catalyst for ORR. The linear sweep voltammetry (LSV) polarization curves were collected using RDE at rotational speed of 1600 rpm. The half-wave potential of $\text{V-Fe}_2\text{P/FePO}_x \text{ @PG}$ catalyst presents a high value of 0.84 V vs. RHE, which is comparable to that of Pt/C catalyst (0.89 V) and outperformed to $\text{Fe}_2\text{P/FePO}_x \text{ @PG}$ (0.80 V) and PG (0.77 V), respectively (Fig. 4b). Moreover, the diffusion-limited current of $\text{V-Fe}_2\text{P/FePO}_x \text{ @PG}$ exhibited as high as $\sim 6.64 \text{ mA cm}^{-2}$, which surpasses the Pt/C (5.65 mA cm^{-2}) and other counterparts of

$\text{Fe}_2\text{P/FePO}_x \text{ @PG}$ (4.69 mA cm^{-2}) and PG (4.03 mA cm^{-2}) (Fig. 4c). The doping of V into $\text{Fe}_2\text{P/FePO}_x \text{ @PG}$ could promote the activation of O_2 molecule on the surface of catalyst, which could increase the ORR process [58]. Moreover, the synergistic effect between V and P, as well as the high crystallinity Fe_2P and amorphous FePO_x active sites in PG framework, effectively accelerated the catalyst for OER and ORR [59]. To deeply understand the real active centers of as-prepared catalysts for ORR, we utilized the SCN^- ions as the reactive agent which could generate the strong bond and poison the Fe-based catalyst during ORR performance [60,61]. Fig. S5 showed the LSV polarization curves of $\text{V-Fe}_2\text{P/FePO}_x \text{ @PG}$ catalyst with the half-wave and onset potential shifted backward to the negative side and diffusion-limiting current density decreased after adding of SCN^- . Remarkably, the $\text{V-Fe}_2\text{P/FePO}_x \text{ @PG}$ catalyst was well-recovered to initial state after raising with water to dissolve the SCN^- [60,61]. This result clarified that the catalysts with Fe active sites play the critical role in the main reaction and enhance the ORR performance. In addition, the Tafel plots illustrate the reaction kinetic of catalysts, which could be derived from the LSV polarization curves, shown in Fig. 4d. The $\text{V-Fe}_2\text{P/FePO}_x \text{ @PG}$ catalyst shows a smallest Tafel slope of 96.2 mV dec^{-1} , which is better than that of $\text{Fe}_2\text{P/FePO}_x \text{ @PG}$, PG, and Pt/C of 152.1, 151.6, and $116.8 \text{ mV dec}^{-1}$, respectively, implying the superior kinetics for ORR of $\text{V-Fe}_2\text{P/FePO}_x \text{ @PG}$. This result is due to the fast electron transport of $\text{V-Fe}_2\text{P/FePO}_x \text{ @PG}$ with tunable nanostructure and synergistic effect that boost the reaction kinetics. To further examine the reaction mechanism, we used rotation ring disk electrode (RRDE), and Fig. 4e shows the obtained LSV curves [62]. The H_2O_2 yield was derived from the LSV curves and showed a value of less than 6% for $\text{V-Fe}_2\text{P/FePO}_x \text{ @PG}$ catalyst, surpassing the counterpart catalysts, such as $\text{Fe}_2\text{P/FePO}_x \text{ @PG}$ (21%), PG (16%), and highly comparable to Pt/C (4%) (Fig. 4f). In addition, the number of electron transfer of $\text{V-Fe}_2\text{P/FePO}_x \text{ @PG}$ catalyst exhibited the value of 3.96, which is very close to the theoretical value of 4, illustrating the ORR following the efficient four-electron reaction mechanism. To investigate the reaction kinetics of the catalysts, we performed the LSV with different rotational speed from 400 to 2500 rpm (Fig. 4g and Fig. S6a,c,e). The limiting current gradually increased with increasing rotation speed, due to the improved convectional mass transfer and diffusion ability of oxygen molecules. The Koutecky–Levich (K–L) plots were determined from the LSV curves at different potential from 0.4 to 0.7 V and are plotted in Fig. 4h and Fig. S6b,d,f. The slope of K–L indicates the electron transferred (n) of $\text{V-Fe}_2\text{P/FePO}_x \text{ @PG}$, $\text{Fe}_2\text{P/FePO}_x \text{ @PG}$, PG, and Pt/C catalysts demonstrated the ORR of catalysts follow the four-electron pathway.

The methanol tolerance measurement was performed by chronoamperometry technique at a fixed potential of -0.3 V . When 10 mL of methanol was added, the $\text{V-Fe}_2\text{P/FePO}_x \text{ @PG}$ catalyst showed almost unchanged current density, demonstrating the susceptibility to the methanol crossover effect (Fig. S7). In contrast, the significant change in current density for Pt/C catalyst exhibited sensitivity towards fuel oxidation. This result further confirmed the high selectivity of $\text{V-Fe}_2\text{P/FePO}_x \text{ @PG}$ catalyst during ORR [63]. Moreover, the long-term stability of catalysts is an important factor for practical application. Fig. 4i shows the chronoamperometric curve of $\text{V-Fe}_2\text{P/FePO}_x \text{ @PG}$ and Pt/C in the same running condition. The $\text{V-Fe}_2\text{P/FePO}_x \text{ @PG}$ catalyst presented an ultralong stability with nearly 95% retention of current density after continuous running for 12 h, which is much better than the benchmark Pt/C catalyst (78% retention) and recent reports of non-noble metal electrocatalysts for ORR in the literature (Table S2). Fig. S8 shows the LSV that was tested after long-term stability. The half-wave potential of $\text{V-Fe}_2\text{P/FePO}_x \text{ @PG}$ catalyst shows a negligible shift after long-term stability, illustrating the enhancement of durability for ORR. The excellent stability of catalyst materials after ORR measurement was further verified by using SEM, TEM, XRD, and Raman analysis (Fig. S9 and S10). After ORR, the amorphous layer shell of V-FePO_x slightly increased due to the reaction with oxygen species and conversion from phosphide to corresponding phosphate, which is well-consistent with

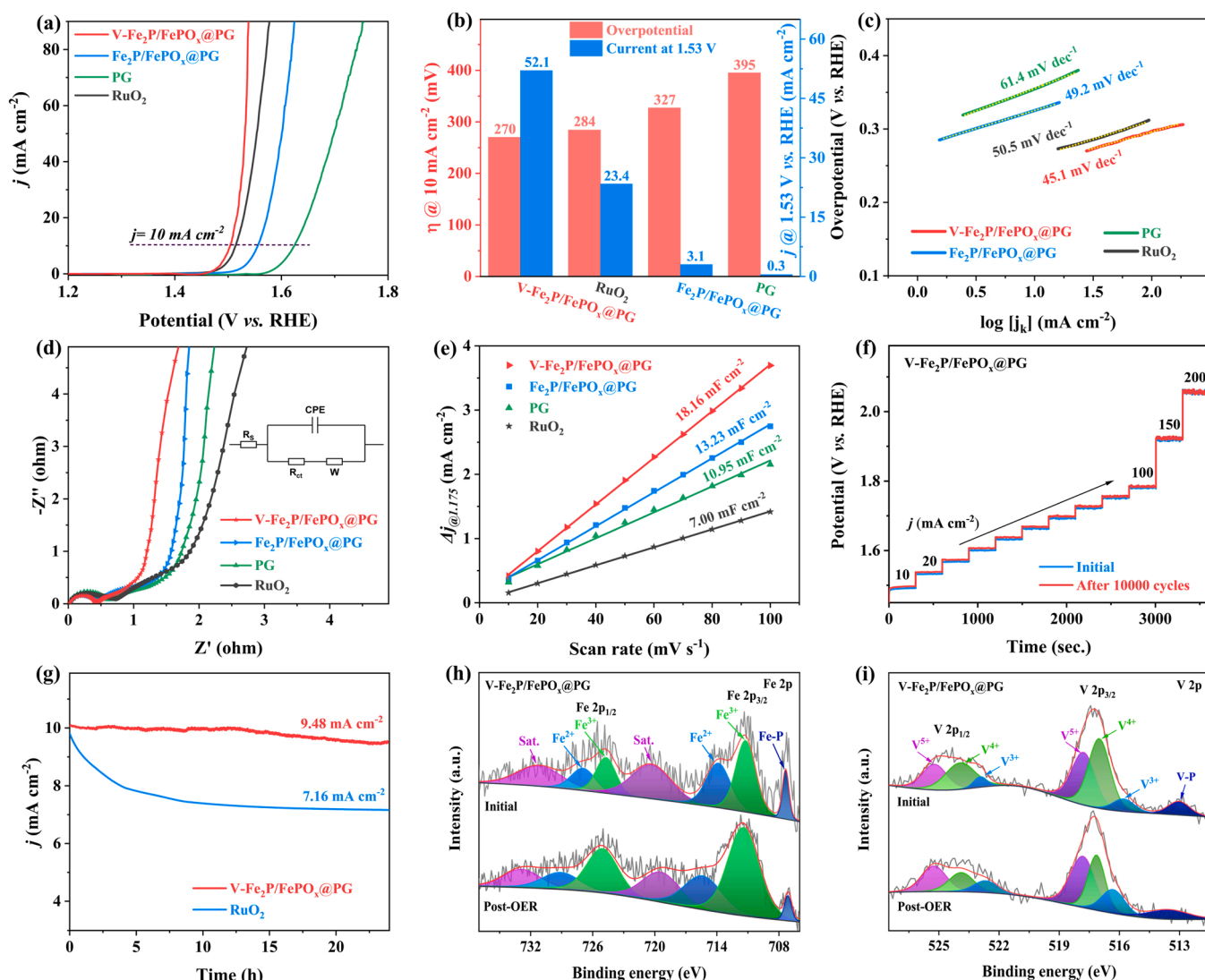


Fig. 5. (a) LSV polarization curves; (b) The overpotential at 10 mA cm^{-2} and current density at 1.53 V comparison; (c) Tafel slope derived from the LSV curves; (d) Nyquist plots; and (e) C_{dl} values of $\text{V-Fe}_2\text{P/FePO}_x @\text{PG}$, $\text{Fe}_2\text{P/FePO}_x @\text{PG}$, PG , and RuO_2 catalysts in 1 M KOH electrolyte; (f) Chronopotentiometry at various current densities of $\text{V-Fe}_2\text{P/FePO}_x @\text{PG}$ catalyst before and after 10000 cycles; (g) Chronoamperometry curves of the $\text{V-Fe}_2\text{P/FePO}_x @\text{PG}$ and RuO_2 at 1.5 V vs. RHE; High-resolution XPS spectra of (h) $\text{Fe } 2p$ and (i) $\text{V } 2p$ for $\text{V-Fe}_2\text{P/FePO}_x @\text{PG}$ catalyst at initial and post-OER performance.

XRD pattern. This excellent stability of catalyst is due to the optimal crystal formation with combination of crystalline and amorphous nanostructure in $\text{V-Fe}_2\text{P/FePO}_x @\text{PG}$. Moreover, to further investigate the effect of PG on the degradation of catalyst during ORR, we performed the stability test of $\text{V-Fe}_2\text{P/FePO}_x @\text{PG}$ with chronoamperometry measurement (Fig. S11). The $\text{V-Fe}_2\text{P/FePO}_x @\text{PG}$ catalyst revealed a better current density retention of 95% in compared to $\text{V-Fe}_2\text{P/FePO}_x$ (86%) after 10 h, demonstrating the outstanding durability of catalyst with the support from PG layer [64,65].

3.2.2. OER performance

The OER performance plays a role in the charging process and energy storage performance of ZABs. Fig. 5a shows the LSV polarization curves for OER of all the catalysts. The $\text{V-Fe}_2\text{P/FePO}_x @\text{PG}$ catalyst displayed a small overpotential of 270 mV , which is better than the state-of-the-art RuO_2 (284 mV), and other comparable catalysts, such as $\text{Fe}_2\text{P/FePO}_x @\text{PG}$ and PG at 327 and 395 mV , respectively (Fig. 5b), and other transition metal catalyst for OER in the literature (Table S3). Moreover, the bare nickel foam showed a high overpotential of 403 mV at current density of 10 mA cm^{-2} , illustrating the small effect on the OER performance (Fig. S12). The Tafel plots illustrate the efficiency of the catalysts'

response when an overpotential was employed; a smaller required overpotential could be demonstrated by a smaller slope [66]. The Tafel slope of $\text{V-Fe}_2\text{P/FePO}_x @\text{PG}$ catalyst shows a small value of 45.1 mV dec^{-1} , which is comparable to the benchmark RuO_2 (50.5 mV dec^{-1}) and other counterparts, such as $\text{Fe}_2\text{P/FePO}_x @\text{PG}$ (49.2 mV dec^{-1}) and PG (61.4 mV dec^{-1}), respectively (Fig. 5c). Electrochemical impedance spectroscopy (EIS) is a powerful technique to examine the catalyst properties and electrode surface. Fig. 5d shows that the charge-transfer resistance of $\text{V-Fe}_2\text{P/FePO}_x @\text{PG}$ catalyst presents a small value of 0.44Ω , which is better than that of $\text{Fe}_2\text{P/FePO}_x @\text{PG}$, PG , and RuO_2 of 0.47 , 0.62 , and 0.73Ω , respectively. The high conductivities of $\text{V-Fe}_2\text{P/FePO}_x @\text{PG}$ catalyst could boost the reaction kinetics and electrochemical performance. Moreover, the catalysts properties were strongly affected by the electrochemical surface areas (ECSAs), which are calculated by calculating the capacitance at a fixed potential range. We have performed the CV at various scan rates in 1 M KOH solution (Fig. S13). The $\text{V-Fe}_2\text{P/FePO}_x @\text{PG}$ catalyst showed a high value of capacitance (C_{dl}) of 18.16 mF cm^{-2} , which is superior to that of $\text{Fe}_2\text{P/FePO}_x @\text{PG}$, PG , and RuO_2 of 13.23 , 10.95 , and 7.00 mF cm^{-2} , respectively (Fig. 5e). The optimal design of the $\text{V-doped Fe}_2\text{P/FePO}_x @\text{PG}$ could significantly enhance the active sites by oxygen coupling

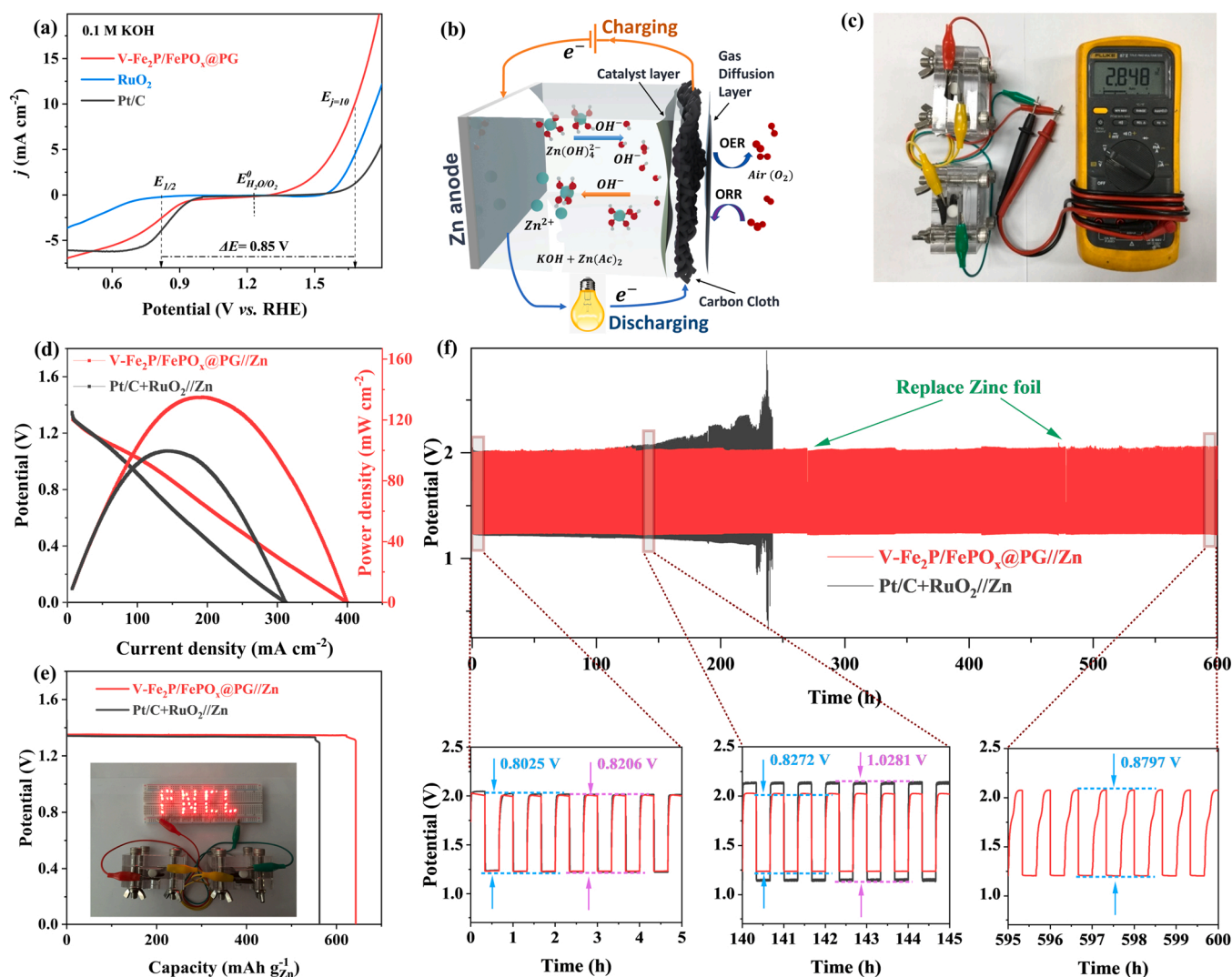


Fig. 6. (a) The LSV curves of V-Fe₂P/FePO_x@PG, RuO₂, and Pt/C for both ORR and OER in 0.1 M KOH; (b) Schematic of the assembled liquid-based rechargeable ZAB; (c) The configurations and OCV of the series-connected batteries; (d) The i - v polarization and power density curves; (e) Specific capacity at a current density of 5 mA cm⁻² (inset showed the batteries powered LEDs); and (f) Cycling stability of the liquid-based rechargeable ZABs with V-Fe₂P/FePO_x@PG and Pt/C + RuO₂ air cathodes.

from the amorphous layer, and graphene as well. The binding between oxygen and metal could boost the intermediate species adsorption, and therefore enhance the conversion reaction. To apply the V-Fe₂P/FePO_x@PG catalyst for ZABs cathode, long-term working ability is necessary. The chronopotentiometry and LSV polarization were measured after long-term stability for 10000 CV cycles, which displayed a small change, compared to the initial curve, confirming the high durability performance (Fig. 5f and S14). In addition, the chronoamperometry was carried out at a fixed potential of 1.5 V vs. RHE for 24 h. Fig. 5g shows that the V-Fe₂P/FePO_x@PG catalyst exhibited excellent OER stability with small current loss, which is much better than RuO₂. Fig. 5h,i show the high-resolution XPS of Fe 2p and V 2p for post-OER. As compared to the initial XPS, after long-term OER measurement, the peak was obtained with negligible change. This result is due to the tunable crystal with an optimal ratio of high crystallinity and amorphous V-Fe₂P/FePO_x@PG. The formation of oxygen binding in FePO_x could generate the intermediate species and stabilize the catalysts nanostructure during OER [67]. Moreover, during the electrochemical performance, the transformation from lower to higher valent state of metal species could boost the true catalyst accessible active sites [68,69]. This process led to increase the diffusion of intermediate species to catalyst surface and accelerate the proton transport mediator [69,70]. The phosphate layer is probably

responsible for promoting the electron/proton transfer and the formation of oxygen-containing substances to boost the oxygen reaction kinetics [71–73].

The SEM, TEM, XRD, and Raman of V-Fe₂P/FePO_x@PG catalyst after long-term OER were analyzed and shown in Fig. S15 and Fig. S16. After OER, the V-Fe₂P core partially oxidized and converted into amorphous shell, which clearly showed the enhancement thickness layer of V-FePO_x (Fig. S15). Furthermore, the XRD after OER demonstrated the intensity increasing of typical V-FePO₄ peak at 2θ ~25.6° (Fig. S16a), further verified the transformation of core V-Fe₂P into shell V-FePO_x and it is consistent with XPS analysis [74,75]. The bifunctional catalyst activities were examined by measuring the LSV polarization for ORR and OER (Fig. 6a). The V-Fe₂P/FePO_x@PG catalyst exhibited a potential difference between half-wave potential (ORR) and over-potential at a current density of 10 mA cm⁻² (OER) as small as 0.85 V, illustrating the outstanding bifunctional catalyst properties. The catalytic activities of V-Fe₂P/FePO_x@PG for ORR outperformed the other non-noble metal catalysts in recent reports (Table S4). The excellent bifunctional catalyst properties of V-Fe₂P/FePO_x@PG are obtained from the following attributes: (i) the optimal design of V-Fe₂P/FePO_x@PG nanostructure with enriched active sites and perfect PG encapsulation; (ii) the four-electron reaction pathway, which increases the

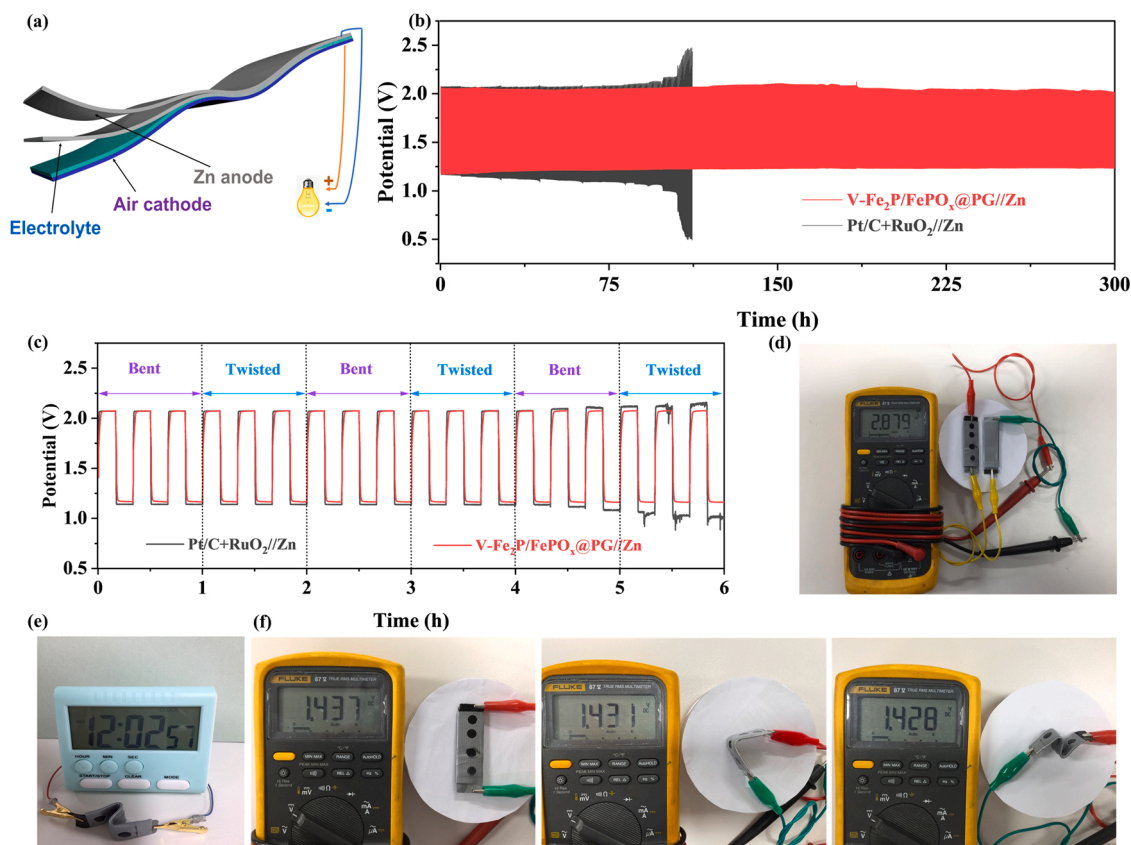


Fig. 7. Electrochemical performance of the rechargeable QSS-ZABs: (a) Schematic illustration of QSS-ZABs; (b) Cycling stability at a current density of 5 mA cm^{-2} ; (c) The charge–discharge curves for different bending and twisting states of rechargeable QSS-ZAB with $\text{V-Fe}_2\text{P/FePO}_x @\text{PG}$ and $\text{Pt/C} + \text{RuO}_2$ air cathodes; (d) The OCV of series-connected flexible QSS ZABs; (e) The clock powered; and (f) The OCV at different bending states of the rechargeable QSS-ZAB.

kinetic and efficiency for ORR and OER by enhancing the transport ability; (iii) the synergistic effect between active metal V and Fe in the phosphide and phosphate nanostructure, which could accelerate the oxygen reactions. For comparison, we coated the as-prepared catalyst material on the carbon cloth substrate and verified the OER performance. As shown in Fig. S17, the OER catalytic activities of $\text{V-Fe}_2\text{P/FePO}_x @\text{PG}$ is superior to other counterparts of $\text{Fe}_2\text{P/FePO}_x @\text{PG}$, PG, and the benchmark RuO_2 catalysts. The results are well-consistent with the evaluation of catalyst performance coated on nickel foam substrate which were described above and additional confirmed the small contribution of nickel foam substrate on the catalytic activities for OER.

3.2.3. Liquid ZABs performance

The excellent ORR and OER performance could open the prospect of applying $\text{V-Fe}_2\text{P/FePO}_x @\text{PG}$ catalyst as an effective air cathode for ZABs. The as-synthesized catalysts were coated on carbon cloth with a gas diffusion layer, and used as a cathode, the alkaline solution consisting of 6 M KOH and 0.2 M $\text{Zn}(\text{ac})_2$ was used as electrolyte, and Zn foil as an anode (Fig. 6b). The ZABs with the cathode fabricated from the mixture of Pt/C and RuO_2 was characterized for comparison. The open circuit potential of two series-connected ZABs were measured as high as 2.848 V, which demonstrated the effectiveness of the air cathode for ZABs of $\text{V-Fe}_2\text{P/FePO}_x @\text{PG}$ catalyst (Fig. 6c). The power density is an important factor for energy storage devices; we investigated the power density of the as-fabricated ZABs. Fig. 6d shows the i - v polarization curves that were measured. The $\text{V-Fe}_2\text{P/FePO}_x @\text{PG}$ -based cathode ZAB showed a high peak power density of 137 mW cm^{-2} at a current density of 191 mA cm^{-2} , which surpasses the Pt/C+RuO_2 cathode-based ZABs (101 mW cm^{-2} at 149 mA cm^{-2}), and the other reported ZABs in the literature (Table S5). Fig. S18 shows the charge/discharge

polarization curves of the ZAB-based $\text{V-Fe}_2\text{P/FePO}_x @\text{PG}$ cathodes, which exhibit a small charge–discharge voltage gap, compared to Pt/C+RuO_2 ZAB, which reveals the high energy efficiency of the $\text{V-Fe}_2\text{P/FePO}_x @\text{PG}$ ZABs. In addition, the $\text{V-Fe}_2\text{P/FePO}_x @\text{PG}$ ZAB displayed a high specific capacity of $642.7 \text{ mAh gZn}^{-1}$ at a current density of 5 mA cm^{-2} , outperforming that of the Pt/C+RuO_2 ZABs of $562.4 \text{ mAh gZn}^{-1}$, and those of the other ZABs in the literature (Fig. 6e, and Table S5). Fig. S19 shows the outstanding rate performance of the $\text{V-Fe}_2\text{P/FePO}_x @\text{PG}$ -based cathode rechargeable ZABs compared to Pt/C+RuO_2 , demonstrating the high ability to work at high current density of the $\text{V-Fe}_2\text{P/FePO}_x @\text{PG}$ cathode-based battery, compared with the Pt/C+RuO_2 . Moreover, two ZABs could successfully power plentiful LEDs, as shown in the inset of Fig. 6e, demonstrating the practical application. To examine the long-term stability of ZAB, we performed the charge–discharge measurement at the current density of 5 mA cm^{-2} . Fig. 6f shows that the $\text{V-Fe}_2\text{P/FePO}_x @\text{PG}$ -based ZAB displays a superior cycle life for 600 h, without any significant decay. The difference between charge and discharge potential represents the energy efficiency of the batteries, which is one of the most important parameters in energy storage devices. After 145 h, the $\text{V-Fe}_2\text{P/FePO}_x @\text{PG}$ ZABs showed a small change in voltage gap from 0.8025 to 0.8272 V, which is superior to that of the Pt/C+RuO_2 ZABs of from 0.8206 to 1.0281 V. In addition, the charge/discharge efficiency was calculated as high as 60.6% at initial stage and still maintain at 59.5% after long-term stability of 600 h, illustrating the excellent performance of as-fabricated ZABs. Moreover, the Pt/C+RuO_2 ZABs could maintain the working ability for more than 200 h, whereas the $\text{V-Fe}_2\text{P/FePO}_x @\text{PG}$ showed a small increase in voltage difference, even after 600 h. Fig. S20 shows the long-term stability of the $\text{V-Fe}_2\text{P/FePO}_x @\text{PG}$ -based ZABs at a high current density of 20 mA cm^{-2} , illustrating the excellent working possibility at high current for a long time. The ultralong cycle life of the $\text{V-Fe}_2\text{P/}$

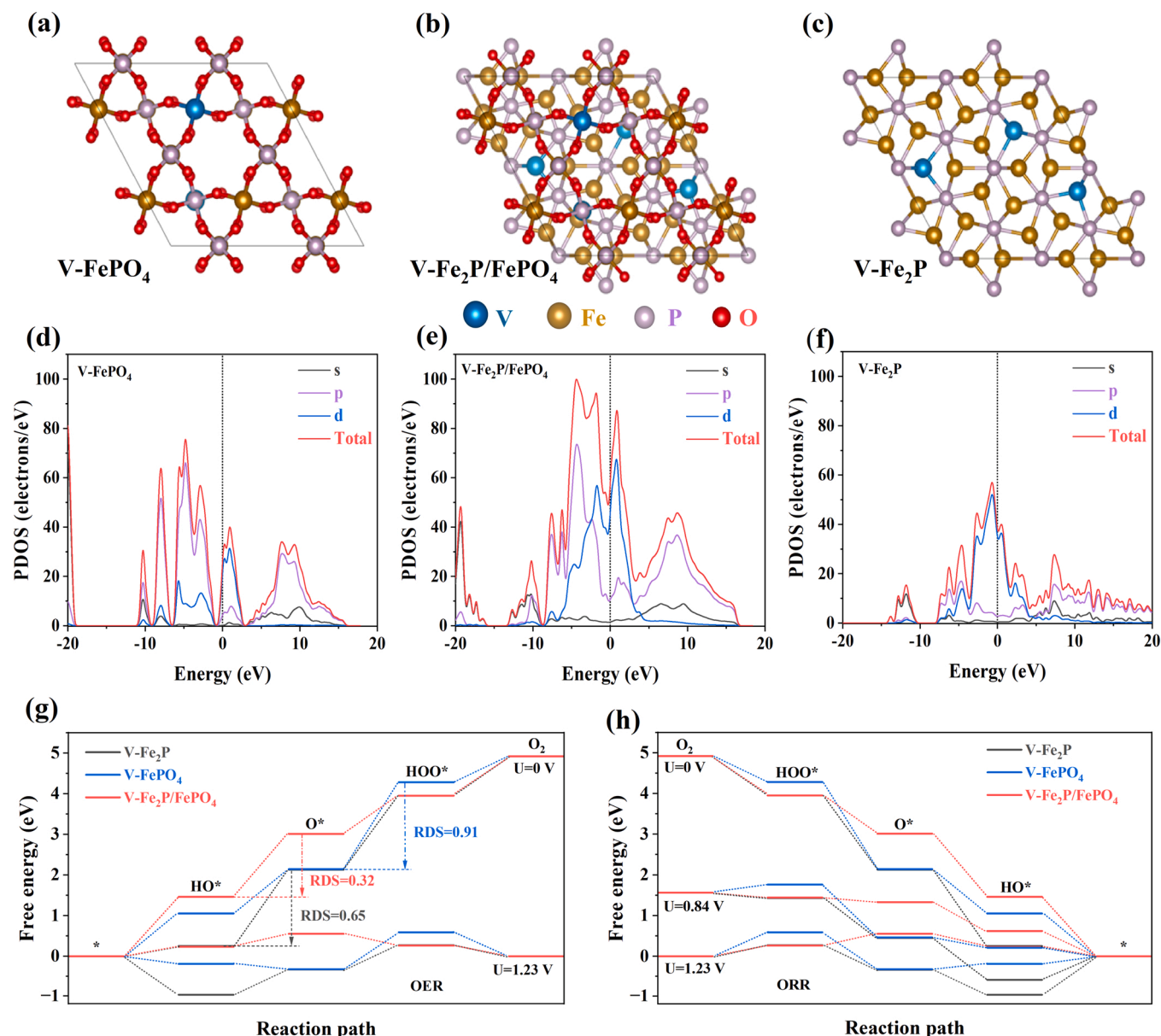


Fig. 8. Structural models for the DFT calculation of (a) V-FePO₄, (b) V-Fe₂P/FePO₄, and (c) V-Fe₂P; (d-f) corresponding PDOS calculation; Free energy of different structural models for (g) OER, and (h) ORR processes.

FePO_x@PG ZABs benefits from the excellent catalytical properties of the catalysts for OER and ORR. The optimized nanostructure of V-Fe₂P/FePO_x@PG, together with the synergistic effect from metal active sites and PG network, could enhance the ZABs performance, and simplify the fabrication process.

3.2.4. Solid state ZABs

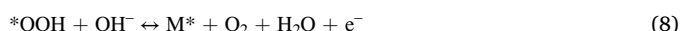
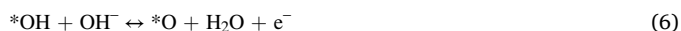
The flexible energy storage system could provide a high opportunity for use in different industrial processes. Herein, we investigated the solid-state ZABs performance with V-Fe₂P/FePO_x@PG as the air cathode, PVA/KOH gel with the additive Zn(ac)₂ as the electrolyte, and a thin Zn foil as an anode. The three components were assembled and wrapped in paraffin film with holes (Fig. 7a). Two connected solid-state ZABs exhibited a long cycle life without degradation after continuously charge-discharge for 300 h. In comparison, the Pt/C+RuO₂-based solid-state ZABs failed after charge-discharge for 100 h (Fig. 7b). Moreover, the charge-discharge performance was performed at different binding and twisting condition for the solid-state ZABs. Fig. 7c shows the

charge-discharge stability the V-Fe₂P/FePO_x@PG-based solid-state ZABs presented at different states after 6 h, which is superior to the comparable Pt/C+RuO₂ ZABs. The high mechanical properties of the as-prepared V-Fe₂P/FePO_x@PG catalysts are due to the combination of the high active site metal phosphide/phosphate and graphene framework, which could improve the stability of the air cathode under different bending/twisting conditions. In addition, two devices of V-Fe₂P/FePO_x@PG-based solid-state ZAB revealed an OCP as high as 2.879 V (Fig. 7d), and were able to power a digital clock at the flexible state (Fig. 7e). The OCP of a single solid-state ZAB was measured at different bending and flexible states, and exhibited negligible change, as Fig. 7f shows. These results further demonstrate that the V-Fe₂P/FePO_x@PG could be effective material to serve as the air cathode for flexible solid-state ZABs and other wearable electronic devices.

3.2.5. Theoretical calculation

The density-functional theory (DFT) first-principle calculation was exploited to deeply understand the electrochemical performance of

V-Fe₂P/FePO₄ @PG catalyst (Fig. 8). The structural models of V-FePO₄, V-Fe₂P/FePO₄, and V-Fe₂P were built and optimized as shown in Fig. 8a-c. The projected density of state (PDOS) for all catalysts were performed and shown in Fig. 8d-f [35–40]. At the Fermi level, the V-Fe₂P/FePO₄ showed a higher density of states in compared to V-Fe₂P and V-FePO₄, demonstrating the sufficient electrical conductivity of heterostructures that could increase the electron transport from core to shell and charge transfer at the catalyst interface. Moreover, the Gibb free energy for the different steps of OER/ORR mechanisms was examined and depicted in Fig. 8g,h. The reaction coordination steps for OER/ORR could follow instinctively reaction pathway [76]:



The rate-determining step (RDS) of reaction was identified as the biggest difference of free energy that could refer to the OER/ORR catalytic activities. At the balance potential state of U = 0 V, the V-Fe₂P/FePO₄ model revealed a small RDS of 0.32 eV, which is better than V-Fe₂P (0.65 eV) and V-FePO₄ (0.91 eV), respectively (Fig. 8g). These results suggested that the core-shell structures of V-Fe₂P/FePO₄ could generate the synergistic effect between V-Fe₂P and V-FePO₄ that accelerate the sluggish reaction during multi-steps for OER and ORR, therefore it could reduce the required overpotential enhance the electrochemical performance of the catalysts.

4. Conclusion

In summary, we have investigated the combination of high-crystallinity Fe₂P and amorphous FePO₄ and the doping effect of V into hybrid nanostructures. A large-scalable and straightforward approach was employed. The synergistic effect and encapsulation formation of metal active sites and graphene network could enhance the catalytical performances of the V-Fe₂P/FePO₄ @PG for ORR and OER. Remarkably, the V-Fe₂P/FePO₄ @PG-based air cathode showed an ultra-high peak power density of 137 mW cm⁻² and long-term stability with negligible degradation after 600 h, superior to the state-of-the-art Pt/C + RuO₂ ZABs. This proposed investigation and strategy could provide a novel and cost-effective method to design and develop a bifunctional electrocatalyst for next-generation energy storages systems with high electrochemical performance and excellent mechanical properties.

CRediT authorship contribution statement

Mr. Quynh Phuong Ngo: Methodology, Investigation, Validation, Formal analysis, Writing – original draft. **Dr. Thanh Tuan Nguyen:** Conceptualization, Writing – review & editing. **Mr. Manjinder Singh:** Supporting Methodology, Investigation, Validation. **Mr. Ravichandran Balaji:** Supporting Methodology, Investigation, Validation. **Prof. Nam Hoon Kim:** Conducting project, Writing – review & editing, supervision. **Prof. Joong Hee Lee:** Conceptualization, writing- reviewing and editing, funding, supervision.

Declaration of Competing Interest

The authors declare that they have no known competing financial interests or personal relationships that could have appeared to influence the work reported in this paper.

Data Availability

Data will be made available on request.

Acknowledgments

This work was supported by the Basic Science Research Program (2022R1A2C2010339) and the Regional Leading Research Center Program (2019R1A5A8080326) through the National Research Foundation funded by the Ministry of Science and ICT of the Republic of Korea.

Appendix A. Supporting information

Supplementary data associated with this article can be found in the online version at doi:10.1016/j.apcatb.2023.122674.

References

- [1] G. Crabtree, Perspective: the energy-storage revolution, *Nature* 526 (2015) S92.
- [2] Q.Y. Jin, B.W. Ren, H. Cui, C.X. Wang, Nitrogen and cobalt co-doped carbon nanotube films as binder-free trifunctional electrode for flexible zinc-air battery and self-powered overall water splitting, *Appl. Catal. B: Environ.* 283 (2021), 119643.
- [3] H. Lei, S. Yang, Q. Wan, L. Ma, M.S. Javed, S. Tan, Z. Wang, W. Mai, Coordination and interface engineering to boost catalytic property of two-dimensional ZIFs for wearable Zn-air batteries, *J. Energy Chem.* 68 (2022) 78–86.
- [4] F. Cheng, J. Chen, Metal-air batteries: from oxygen reduction electrochemistry to cathode catalysts, *Chem. Soc. Rev.* 41 (2012) 2172–2192.
- [5] Y. Chen, T. He, Q. Liu, Y. Hu, H. Gu, L. Deng, H. Liu, Y. Liu, Y.-N. Liu, Y. Zhang, S. Chen, X. Ouyang, Highly durable iron single-atom catalysts for low-temperature zinc-air batteries by electronic regulation of adjacent iron nanoclusters, *Appl. Catal. B: Environ.* (2022), 122163.
- [6] H. Lei, L. Ma, Q. Wan, Z. Huangfu, S. Tan, Z. Wang, W. Mai, Porous carbon nanofibers confined NiFe alloy nanoparticles as efficient bifunctional electrocatalysts for Zn-air batteries, *Nano Energy* 104 (2022), 107941.
- [7] Y.-f. Cui, Y.-h. Zhu, J.-y. Du, Y.-l. Zhang, K. Li, W.-q. Liu, G. Huang, X.-b. Zhang, A high-voltage and stable zinc-air battery enabled by dual-hydrophobic-induced proton shuttle shielding, *Joule* 6 (2022) 1617–1631.
- [8] Z.F. Huang, J. Wang, Y.C. Peng, C.Y. Jung, A. Fisher, X. Wang, Design of efficient bifunctional oxygen reduction/evolution electrocatalyst: recent advances and perspectives, *Adv. Energy Mater.* 7 (2017) 1700544.
- [9] Y. Zhang, D. Wu, F. Huang, Y. Cai, Y. Li, H. Ke, P. Lv, Q. Wei, “Water-in-Salt” Nonalkaline gel polymer electrolytes enable flexible zinc-air batteries with ultra-long operating time, *Adv. Funct. Mater.* 32 (2022) 2203204.
- [10] C.F. Huang, Y.S. Zhang, X.W. Li, H.J. Cao, Y.M. Guo, C.H. Zhang, Mn-incorporated Co₃O₄ bifunctional electrocatalysts for zinc-air battery application: an experimental and DFT study, *Appl. Catal. B: Environ.* 319 (2022), 121909.
- [11] J.H. Song, C.Z. Zhu, B.Z. Xu, S.F. Fu, M.H. Engelhard, R.F. Ye, D. Du, S.P. Beckman, Y.H. Lin, Bimetallic cobalt-based phosphide zeolitic imidazolate framework: CoP_x phase-dependent electrical conductivity and hydrogen atom adsorption energy for efficient overall water splitting, *Adv. Energy Mater.* 7 (2017) 1601555.
- [12] H. Ji, M. Wang, S. Liu, H. Sun, J. Liu, T. Qian, C. Yan, In-situ observation as activity descriptor enables rational design of oxygen reduction catalyst for zinc-air battery, *Energy Store Mater.* 27 (2020) 226–231.
- [13] M. Singh, T.T. Nguyen, M.A. P. Q.P. Ngo, D.H. Kim, N.H. Kim, J.H. Lee, Metallic metastable hybrid 1T'/1T phase triggered Co₂P-SnS₂ nanosheets for high efficiency trifunctional electrocatalyst, *Small* (2023) 2206726.
- [14] W.W. Tian, J.T. Ren, Z.Y. Yuan, In-situ cobalt-nickel alloy catalyzed nitrogen-doped carbon nanotube arrays as superior freestanding air electrodes for flexible zinc-air and aluminum-air batteries, *Appl. Catal. B: Environ.* 317 (2022), 121764.
- [15] S. Li, B. Chen, Y. Wang, M.Y. Ye, P.A. van Aken, C. Cheng, A. Thomas, Oxygen-evolving catalytic atoms on metal carbides, *Nat. Mater.* 20 (2021) 1240–1247.
- [16] C.C. McCrory, S. Jung, J.C. Peters, T.F. Jaramillo, Benchmarking heterogeneous electrocatalysts for the oxygen evolution reaction, *J. Am. Chem. Soc.* 135 (2013) 16977–16987.
- [17] M.R. Kandel, U.N. Pan, D.R. Paudel, P.P. Dhakal, N.H. Kim, J.H. Lee, Hybridized bimetallic phosphides of Ni–Mo, Co–Mo, and Co–Ni in a single ultrathin-3D-nanosheets for efficient HER and OER in alkaline media, *Compos. B. Eng.* 239 (2022), 109992.
- [18] X.T. Han, N.N. Li, P.X. Xiong, Y.B. Kang, Q.Y. Dou, Q. Liu, W.W. Li, J.Y. Lee, H. S. Park, Rhenium induced electronic structure modulation of Ni₃S₂/N-doped graphene for efficient trifunctional electrocatalysis, *Compos. B. Eng.* 234 (2022), 109670.
- [19] P.K.L. Tran, M.S. Kim, T.H. Nguyen, D.T. Tran, N.H. Kim, J.H. Lee, Interfacial engineering for design of novel 2D cobalt sulfide-Mxene heterostructured catalyst toward alkaline water splitting, *Funct. Compos. Struct.* 3 (2021), 045005.
- [20] J. Balamurugan, T.T. Nguyen, D.H. Kim, N.H. Kim, J.H. Lee, 3D nickel molybdenum oxyselenide (Ni_{1-x}Mo_xOSe) nanoarchitectures as advanced multifunctional catalyst for Zn-air batteries and water splitting, *Appl. Catal. B: Environ.* 286 (2021), 119909.

- [21] M. Wang, H. Ji, S. Liu, H. Sun, J. Liu, C. Yan, T. Qian, Single-atom scale metal vacancy engineering in heteroatom-doped carbon for rechargeable zinc-air battery with reduced overpotential, *Chem. Eng. J.* 393 (2020), 124702.
- [22] C.Y. Su, H. Cheng, W. Li, Z.Q. Liu, N. Li, Z.F. Hou, F.Q. Bai, H.X. Zhang, T.Y. Ma, Atomic modulation of feco-nitrogen-carbon bifunctional oxygen electrodes for rechargeable and flexible all-solid-state zinc-air battery, *Adv. Energy Mater.* 7 (2017) 1602420.
- [23] S. Liu, H. Ji, M. Wang, H. Sun, J. Liu, C. Yan, T. Qian, Atomic metal vacancy modulation of single-atom dispersed Co/N/C for highly efficient and stable air cathode, *ACS Appl. Mater. Inter.* 12 (2020) 15298–15304.
- [24] K. Gong, F. Du, Z. Xia, M. Durstock, L. Dai, Nitrogen-doped carbon nanotube arrays with high electrocatalytic activity for oxygen reduction, *Science* 323 (2009) 760–764.
- [25] J. Zhang, Z. Zhao, Z. Xia, L. Dai, A metal-free bifunctional electrocatalyst for oxygen reduction and oxygen evolution reactions, *Nat. Nanotechnol.* 10 (2015) 444–452.
- [26] Q. Zhang, F. Luo, X. Long, X.X. Yu, K.G. Qu, Z.H. Yang, N. P doped carbon nanotubes confined WN-Ni Mott-Schottky heterogeneous electrocatalyst for water splitting and rechargeable zinc-air batteries, *Appl. Catal. B: Environ.* 298 (2021), 120511.
- [27] Q. Shi, Q. Liu, Y. Zheng, Y. Dong, L. Wang, H. Liu, W. Yang, Controllable construction of bifunctional Co_xP@N,P-doped carbon electrocatalysts for rechargeable zinc-air batteries, *Energy Environ. Materials* 5 (2022) 515–523.
- [28] Z. Lu, B. Wang, Y. Hu, W. Liu, Y. Zhao, R. Yang, Z. Li, J. Luo, B. Chi, Z. Jiang, M. Li, S. Mu, S. Liao, J. Zhang, X. Sun, An isolated zinc-cobalt atomic pair for highly active and durable oxygen reduction, *Angew. Chem. Int. Ed.* 58 (2019) 2622–2626.
- [29] S. Ramakrishnan, D.B. Velusamy, S. Sengodan, G. Nagaraju, D.H. Kim, A.R. Kim, D. J. Yoo, Rational design of multifunctional electrocatalyst: an approach towards efficient overall water splitting and rechargeable flexible solid-state zinc-air battery, *Appl. Catal. B: Environ.* 300 (2022), 120752.
- [30] Y.A. Zhang, Y.J. Chen, M. Alfred, F.L. Huang, S.Q. Liao, D.S. Chen, D.W. Li, Q. F. Wei, Alkaline sodium polyacrylate-starch hydrogels with tolerance to cold conditions for stretchable zinc-air batteries, *Compos. B. Eng.* 224 (2021), 109228.
- [31] J. Shi, X. Guo, S. Liu, Y. Sun, J. Zhang, Y. Liu, X. Zheng, Q. Kong, An altered nanoemulsion assembly strategy for in-situ synthesis of Co₂P/NP-C nanospheres as advanced oxygen reduction electrocatalyst for zinc-air batteries, *Compos. Part B: Eng.* 231 (2022), 109589.
- [32] W. Liu, H. Liu, L.N. Dang, H.X. Zhang, X.L. Wu, B. Yang, Z.J. Li, X.W. Zhang, L. C. Lei, S. Jin, Amorphous cobalt-iron hydroxide nanosheet electrocatalyst for efficient electrochemical and photo-electrochemical oxygen evolution, *Adv. Funct. Mater.* 27 (2017) 1603904.
- [33] T.T. Nguyen, J. Balamurugan, K.T. Lau, N.H. Kim, J.H. Lee, Novel cobalt-doped molybdenum oxynitride quantum dot@N-doped carbon nanosheets with abundant oxygen vacancies for long-life rechargeable zinc-air batteries, *J. Mater. Chem. A* 9 (2021) 9092–9104.
- [34] T.T. Nguyen, J. Balamurugan, D.H. Kim, N.H. Kim, J.H. Lee, Hierarchical 3D oxygenated cobalt vanadium selenide nanosheets as advanced electrode for flexible zinc-cobalt and zinc-air batteries, *Small* 16 (2020) 2004661.
- [35] S.J. Clark, M.D. Segall, C.J. Pickard, P.J. Hasnip, M.I.J. Probert, K. Refson, M. C. Payne, First principles methods using CASTEP, *Z. Krist. Cryst. Mater.* 220 (2005) 567–570.
- [36] G.P. Francis, M.C. Payne, Finite basis set corrections to total energy pseudopotential calculations, *J. Phys. Condens. Matter* 2 (1990) 4395–4404.
- [37] P. Hohenberg, W. Kohn, Inhomogeneous electron gas, *Phys. Rev.* 136 (1964) B864–B871.
- [38] W. Kohn, L.J. Sham, Self-consistent equations including exchange and correlation effects, *Phys. Rev.* 140 (1965) A1133–A1138.
- [39] M.C. Payne, M.P. Teter, D.C. Allan, T.A. Arias, J.D. Joannopoulos, Iterative minimization techniques for ab initio total-energy calculations: molecular dynamics and conjugate gradients, *Rev. Mod. Phys.* 64 (1992) 1045–1097.
- [40] B.G. Pfrommer, M. Cote, S.G. Louie, M.L. Cohen, Relaxation of crystals with the quasi-Newton, Method, *J. Comput. Phys.* 131 (1997) 233–240.
- [41] M. Wang, Y. Li, J. Fang, C.J. Villa, Y. Xu, S. Hao, J. Li, Y. Liu, C. Wolverton, X. Chen, Superior oxygen reduction reaction on phosphorus-doped carbon dot/graphene aerogel for all-solid-state flexible air-batteries, *Adv. Energy Mater.* 10 (2020) 1902736.
- [42] G. Zhang, G. Wang, Y. Liu, H. Liu, J. Qu, J. Li, Highly active and stable catalysts of phytic acid-derivative transition metal phosphides for full water splitting, *J. Am. Chem. Soc.* 138 (2016) 14686–14693.
- [43] A.S. Wang, C.N. Zhao, M. Yu, W.C. Wang, Trifunctional Co nanoparticle confined in defect-rich nitrogen-doped graphene for rechargeable Zn-air battery with a long lifetime, *Appl. Catal. B: Environ.* 281 (2021), 119514.
- [44] Z. Sun, M. Zhu, X. Lv, Y. Liu, C. Shi, Y. Dai, A. Wang, T. Majima, Insight into iron group transition metal phosphides (Fe₂P, Co₂P, Ni₂P) for improving photocatalytic hydrogen generation, *Appl. Catal. B: Environ.* 246 (2019) 330–336.
- [45] F. Yang, X.X. Fan, C.X. Wang, W. Yang, L.Q. Hou, X.W. Xu, A.D. Feng, S. Dong, K. Chen, Y. Wang, Y.F. Li, P-doped nanomesh graphene with high-surface-area as an efficient metal-free catalyst for aerobic oxidative coupling of amines, *Carbon* 121 (2017) 443–451.
- [46] T.T. Nguyen, J. Balamurugan, H.W. Go, Q.P. Ngo, N.H. Kim, J.H. Lee, Dual-functional Co_{5.47}N/Fe₃N heterostructure interconnected 3D N-doped carbon nanotube-graphene hybrids for accelerating polysulfide conversion in Li-S batteries, *J. Chem. Eng.* 427 (2022), 131774.
- [47] O.-K. Park, N.H. Kim, J.H. Lee, Rapid effective reduction by microwave-irradiated thermal reaction for large-scale production of high-quality reduced graphene oxide, *Carbon* 187 (2022) 330–337.
- [48] M.S. Yun, T.H. Nguyen, D.T. Tran, N.H. Kim, J.H. Lee, Ultrasmall molybdenum-iron nitride nanoparticles confined carbon nanotubes hybrids for efficient overall water splitting, *Funct. Compos. Struct.* 4 (2022).
- [49] D. Gu, W. Schmidt, C.M. Pichler, H.J. Bongard, B. Spliethoff, S. Asahina, Z. Cao, O. Terasaki, F. Schuth, Surface-casting synthesis of mesoporous zirconia with a cmk-5-like structure and high surface area, *Angew. Chem. Int. Ed.* 56 (2017) 11222–11225.
- [50] M. Borghei, J. Lehtonen, L. Liu, O.J. Rojas, Advanced biomass-derived electrocatalysts for the oxygen reduction reaction, *Adv. Mater.* 30 (2018), e1703691.
- [51] X.Y. Zhang, F.T. Li, Z.N. Shi, B. Dong, Y.W. Dong, Z.X. Wu, L. Wang, C.G. Liu, Y. M. Chai, Vanadium doped FeP nanoflower with optimized electronic structure for efficient hydrogen evolution, *J. Colloid Interface Sci.* 615 (2022) 445–455.
- [52] K.P. Singh, E.J. Bae, J.S. Yu, Fe-P: a new class of electroactive catalyst for oxygen reduction reaction, *J. Am. Chem. Soc.* 137 (2015) 3165–3168.
- [53] R. Li, Z.D. Wei, X.L. Gou, W. Xu, Phosphorus-doped graphene nanosheets as efficient metal-free oxygen reduction electrocatalysts, *RSC Adv.* 3 (2013) 9978–9984.
- [54] T.W. Zhao, X.J. Shen, Y. Wang, R.K. Hocking, Y.B. Li, C.L. Rong, K. Dastafkan, Z. Su, C. Zhao, In situ reconstruction of v-doped Ni₂P pre-catalysts with tunable electronic structures for water oxidation, *Adv. Funct. Mater.* 31 (2021) 2100614.
- [55] Z.W. Liu, J. Ai, M.M. Sun, F. Han, Z.K. Li, Q.C. Peng, Q.D. Wang, J.L. Liu, L. Liu, Phosphorous-doped graphite layers with outstanding electrocatalytic activities for the oxygen and hydrogen evolution reactions in water electrolysis, *Adv. Funct. Mater.* 30 (2020) 1910741.
- [56] Y.H. Seon, R. Saroha, J.S. Cho, Hierarchically porous N-doped C nanofibers comprising TiO₂ quantum dots and ZIF-8-derived hollow C nanocages as ultralight interlayer for stable Li-S batteries, *Compos. B. Eng.* 237 (2022), 109856.
- [57] D.H. Guo, R. Shibuya, C. Akiba, S. Saji, T. Kondo, J. Nakamura, Active sites of nitrogen-doped carbon materials for oxygen reduction reaction clarified using model catalysts, *Science* 351 (2016) 361–365.
- [58] X.L. Xing, R.J. Liu, M. Anjass, K.C. Cao, U. Kaiser, G.J. Zhang, C. Streb, Bimetallic manganese-vanadium functionalized N,S-doped carbon nanotubes as efficient oxygen evolution and oxygen reduction electrocatalysts, *Appl. Catal. B: Environ.* 277 (2020), 119195.
- [59] L. Dai, Y. Xue, L. Qu, H.J. Choi, J.B. Baek, Metal-free catalysts for oxygen reduction reaction, *Chem. Rev.* 115 (2015) 4823–4892.
- [60] F.-L. Meng, Z.-L. Wang, H.-X. Zhong, J. Wang, J.-M. Yan, X.-B. Zhang, Reactive multifunctional template-induced preparation of Fe-N-doped mesoporous carbon microspheres towards highly efficient electrocatalysts for oxygen reduction, *Adv. Mater.* 28 (2016) 7948–7955.
- [61] K. Yuan, D. Lützenkirchen-Hecht, L. Li, L. Shuai, Y. Li, R. Cao, M. Qiu, X. Zhuang, M.K.H. Leung, Y. Chen, U. Scherf, Boosting oxygen reduction of single iron active sites via geometric and electronic engineering: nitrogen and phosphorus dual coordination, *J. Am. Chem. Soc.* 142 (2020) 2404–2412.
- [62] L. Wang, J. Cheng, Q.S. Kang, R. Wang, J.F. Ruan, L.X. Li, L.X. Wu, Z.M. Li, N. Ai, Cobalt-containing nanoparticles embedded in flexible carbon aerogel for spilled oil cleanup and oxygen reduction reaction, *Compos. B. Eng.* 174 (2019), 107039.
- [63] H. Yin, C.Z. Zhang, F. Liu, Y.L. Hou, Hybrid of iron nitride and nitrogen-doped graphene aerogel as synergistic catalyst for oxygen reduction reaction, *Adv. Funct. Mater.* 24 (2014) 2930–2937.
- [64] P. Thangasamy, S. Oh, H. Randriamahazaka, S. Nam, I.-K. Oh, Mechanistic insight into collectively exhaustive CoPi-NPC nanosheets for oxygen reduction reaction and Zn-air battery, *Appl. Catal. B: Environ.* 316 (2022), 121656.
- [65] M. Zhang, Y. Xu, H. Zhang, Z. Duan, T. Ren, Z. Wang, X. Li, L. Wang, H. Wang, Synergistic coupling of P-doped Pd₄S nanoparticles with P/S-co-doped reduced graphene oxide for enhanced alkaline oxygen reduction, *J. Chem. Eng.* 429 (2022), 132194.
- [66] K.R. Park, D.T. Tran, T.T. Nguyen, N.H. Kim, J.H. Lee, Copper-Incorporated heterostructures of amorphous NiSe₂/Crystalline NiSe₂ as an efficient electrocatalyst for overall water splitting, *J. Chem. Eng.* 422 (2021), 130048.
- [67] F. Yu, H. Zhou, Y. Huang, J. Sun, F. Qin, J. Bao, W.A. Goddard 3rd, S. Chen, Z. Ren, High-performance bifunctional porous non-noble metal phosphide catalyst for overall water splitting, *Nat. Commun.* 9 (2018) 2551.
- [68] L.-A. Stern, L. Feng, F. Song, X. Hu, Ni₂P as a Janus catalyst for water splitting: the oxygen evolution activity of Ni₂P nanoparticles, *Energy Environ. Sci.* 8 (2015) 2347–2351.
- [69] J. Ryu, N. Jung, J.H. Jang, H.-J. Kim, S.J. Yoo, In situ transformation of hydrogen-evolving CoP nanoparticles: toward efficient oxygen evolution catalysts bearing dispersed morphologies with Co-oxo/hydroxo molecular units, *ACS Catal.* 5 (2015) 4066–4074.
- [70] E. Mirzakulova, R. Khatmullin, J. Walpita, T. Corrigan, N.M. Vargas-Barbosa, S. Vyas, S. Oottikkal, S.F. Manzer, C.M. Hadad, K.D. Glusac, Electrode-assisted catalytic water oxidation by a flavin derivative, *Nat. Chem.* 4 (2012) 794–801.
- [71] M.W. Kanan, D.G. Nocera, In situ formation of an oxygen-evolving catalyst in neutral water containing phosphate and Co²⁺, *Science* 321 (2008) 1072–1075.
- [72] Q. Yin, J.M. Tan, C. Besson, Y.V. Geletii, D.G. Musaev, A.E. Kuznetsov, Z. Luo, K. I. Hardcastle, C.L. Hill, A fast soluble carbon-free molecular water oxidation catalyst based on abundant metals, *Science* 328 (2010) 342–345.
- [73] T.R. Cook, D.K. Dogutan, S.Y. Reece, Y. Surendranath, T.S. Teets, D.G. Nocera, Solar energy supply and storage for the legacy and nonlegacy worlds, *Chem. Rev.* 110 (2010) 6474–6502.
- [74] K.J. May, C.E. Carlton, K.A. Stoerzinger, M. Risch, J. Suntivich, Y.-L. Lee, A. Grimaud, Y. Shao-Horn, Influence of oxygen evolution during water oxidation

- on the surface of perovskite oxide catalysts, *J. Phys. Chem. Lett.* 3 (2012) 3264–3270.
- [75] X. Zhang, J. Zhang, B. Xu, K. Wang, X.W. Sun, Synergistic effects in biphasic nanostructured electrocatalyst: crystalline core versus amorphous shell, *Nano Energy* 41 (2017) 788–797.
- [76] H.W. Go, T.T. Nguyen, Q.P. Ngo, R. Chu, N.H. Kim, J.H. Lee, Tailored heterojunction active sites for oxygen electrocatalyst promotion in zinc-air batteries, *Small* (2023) 2206341.